Journal of Materials Chemistry C

PAPER

View Article Online
View Journal | View Issue

Cite this: J. Mater. Chem. C, 2017, 5, 2368

Ultralow bandgap molecular semiconductors for ambient-stable and solution-processable ambipolar organic field-effect transistors and inverters†

Resul Ozdemir,‡[a] Donghee Choi,‡[b] Mehmet Ozdemir,[a] Guhyun Kwon,[b] Hyekyoung Kim,[b] Unal Sen,[c] Choongik Kim*[b] and Hakan Usta*[a]

The design and development of novel ambipolar semiconductors is very crucial to advance various optoelectronic technologies including organic complementary (CMOS) integrated circuits. Although numerous high-performance ambipolar polymers have been realized to date, small molecules have been unable to provide high ambipolar performance in combination with ambient-stability and solution-processibility. In this study, by implementing highly π-electron deficient, ladder-type **IFDK/IFDM** acceptor cores with bithiophene donor units in D–A–D π-architectures, two novel small molecules, **2OD-TTIFDK** and **2OD-TTIFDM**, were designed, synthesized and characterized in order to achieve ultralow band-gap (1.21–1.65 eV) semiconductors with sufficiently balanced molecular energetics for ambipolarity. The HOMO/LUMO energies of the new semiconductors are found to be −5.47/−3.61 and −5.49/−4.23 eV, respectively. Bottom-gate/top-contact OFETs fabricated *via* solution-shearing of **2OD-TTIFDM** yield perfectly ambient stable ambipolar devices with reasonably balanced electron and hole mobilities of 0.13 $cm^2\ V^{-1}\ s^{-1}$ and 0.01 $cm^2\ V^{-1}\ s^{-1}$, respectively with I_{on}/I_{off} ratios of $\sim 10^3$–10^4, and **2OD-TTIFDK**-based OFETs exhibit ambipolarity under vacuum with highly balanced ($\mu_e/\mu_h \sim 2$) electron and hole mobilities of 0.02 $cm^2\ V^{-1}\ s^{-1}$ and 0.01 $cm^2\ V^{-1}\ s^{-1}$, respectively with I_{on}/I_{off} ratios of $\sim 10^5$–10^6. Furthermore, complementary-like inverter circuits were demonstrated with the current ambipolar semiconductors resulting in high voltage gains of up to 80. Our findings clearly indicate that ambient-stability of ambipolar semiconductors is a function of molecular orbital energetics without being directly related to a bulk π-backbone structure. To the best of our knowledge, considering the processing, charge-transport and inverter characteristics, the current semiconductors stand out among the best performing ambipolar small molecules in the OFET and CMOS-like circuit literature. Our results provide an efficient approach in designing ultralow band-gap ambipolar small molecules with good solution-processibility and ambient-stability for various optoelectronic technologies, including CMOS-like integrated circuits.

Received 22nd November 2016,
Accepted 7th February 2017

DOI: 10.1039/c6tc05079d

rsc.li/materials-c

Introduction

Ambipolar organic semiconductors are attractive functional materials as potential alternatives to conventional inorganic semiconductors (*i.e.*, Si, Ge, GaAs, *etc.*), both for fundamental research and for the fabrication of flexible, low-cost, and light-weight optoelectronic devices such as single-component CMOS (complementary metal-oxide semiconductor)-type transistor circuits and light-emitting transistors (OLETs).[1–8] Device optimizations such as dielectric surface treatments,[9] electrode surface modifications,[10] and use of non-symmetric work-function electrodes,[11] or depositing bilayer/blend semiconductor films[12–14] have been successfully employed to realize ambipolar charge-transport in organic field-effect transistors (OFETs). However, the most ideal approach would be to have an intrinsically ambipolar π-system, regardless

[a] Department of Materials Science and Nanotechnology Engineering, Abdullah Gül University, Kayseri, Turkey. E-mail: hakan.usta@agu.edu.tr
[b] Department of Chemical and Biomolecular Engineering, Sogang University, Mapo-gu, Seoul, Korea. E-mail: choongik@sogang.ac.kr
[c] Department of Mechanical Engineering, Abdullah Gül University, Kayseri, Turkey

† Electronic supplementary information (ESI) available: Synthetic procedures and characterizations for the compounds 2-octyldodecyl bromide and 2,8-dibromo-indeno[1,2-*b*]fluorene-6,12-dione (**IFDK-Br2**) shown in Scheme S1, Fig. S1–S8 ($^1H/^{13}C$ NMR, MALDI-TOF, and ATR-FTIR spectra, TGA/DSC curves of **2OD-TTIFDK** and **2OD-TTIFDM**), Fig. S9 (chemical structures and optimized geometries of some reference compounds), and Fig. S10–S14 (OFET and Inverter electrical curves). See DOI: 10.1039/c6tc05079d

‡ These authors contributed equally to this work.

of the device architecture.[1,15] The ability of an intrinsic ambipolar semiconductor to transport both electrons and holes, as an initial approximation, usually requires energetically close HOMO and LUMO frontier orbitals (energy gap < 2.0 eV), which are symmetrically positioned around the metal electrode fermi level, and also require good solid-state orbital overlaps between neighboring π-systems.[12,16,17] In order to utilize ambipolar semiconductors in ideal optoelectronic applications, charge transport of electrons and holes should be balanced ($\mu_e/\mu_h \approx 1$) with good mobility and ambient stability. This is particularly important to achieve maximum gains in logic circuits and light-emission efficiencies in OLETs. In addition, in order to enable low-cost, facile device fabrications *via* spin-coating, solution-shearing, and printing, the semiconductors should exhibit good solubilities in common organic solvents.

To date, ambient-stable and solution-processable ambipolar semiconductors have been mainly reported with π-conjugated polymers, and charge carrier mobilities exceeding those of amorphous silicon ($\mu_{e,h} > 0.5$ cm^2 V^{-1} s^{-1}) have been achieved in polymer-based organic field-effect transistors (OFETs).[18–20] Most of these polymers have highly extended donor–acceptor (D–A) type π-backbones, which leads to π-electronic structures with small HOMO–LUMO energy gaps (<2.0 eV) and low LUMO energies (<-4.0 eV) to facilitate charge injection/transport of both electrons and holes under ambient conditions.[21–23] Nevertheless, very few solution-processed small molecules with ambipolar charge-transport are known to operate under ambient conditions.[24–26] This is mainly due to the difficulty of achieving such low HOMO–LUMO energy gaps and sufficiently low LUMOs within a limited π-extension of the molecular backbone. When compared with polymers, small molecular π-conjugated systems offer advantageous properties including enhanced solubility, higher crystallinity, better synthetic reproducibility, and higher degree of purity.[27–31] Since the early studies on hole-transporting thiophene-based small molecules in OFETs,[32] the design and development of novel molecular π-architectures with solution-processability and ambient-stability have been quite important for the realization of printed electronic circuits which can operate under ambient conditions.[33–37] To date, many high mobility (>1.0 cm^2 V^{-1} s^{-1}) unipolar (p-channel or n-channel) molecular semiconductors have been developed;[38,39] however, there are very few ambipolar small molecules exhibiting good solution-processibility and ambient stability.[40–42] In addition, the majority of these ambipolar small molecules are based on diketopyrrolopyrrole (DPP) acceptor cores, and they typically have electron/hole mobilities in the range of $\sim$0.001–0.1 cm^2 V^{-1} s^{-1}.[43,44] To the best of our knowledge, the highest ambient-stable electron mobility reported to date was for an ambipolar DPP-based small molecule with μ_e = 0.6–0.8 cm^2 V^{-1} s^{-1}; however, this molecule exhibited a much lower hole mobility of $\sim 10^{-3}$ cm^2 V^{-1} s^{-1} for the same device.[45] Therefore, the continued research efforts to design and develop new ambipolar small molecules are crucial to realize high and balanced charge carrier mobilities, to fully reveal their technological potential and to elucidate the fundamentals of electron *vs.* hole transport processes in novel molecular solids.

To achieve a reasonably balanced ambipolarity in a small molecular backbone, we utilized the strategy of building a very strong D–A–D π-architecture using ladder-type indeno[1,2-*b*]-fluorene-(6,12-dione (**IFDK**) and indeno[1,2-*b*]fluorene-6,12-diylidene)dimalononitrile (**IFDM**) π–acceptors and α-substituted bithiophene terminal π–donor units.[46] This approach can yield very small HOMO–LUMO gaps since the HOMO is dominated by the π–donor unit while the LUMO is dominated by the π–acceptor unit. In addition, the structural and electronic properties of cyclopenta-fused scaffolds can be favorable to stabilize both positive and negative charges on these new molecular backbones.[47] Specifically, **IFDM** was used due to its great coplanarity and extremely strong electron-accepting ability in a proper sized π–core.[48] Swallow-tailed alkyl substitutents, 2-octyldodecyl (2-OD), are placed at molecular termini (α,ω-positions) to ensure good solubility while minimizing inter-ring twists.[49] We report herein the design, synthesis and characterization of two new ladder-type small molecules, 2,8-bis(5′-(2-octyldodecyl)-2,2′-bithiophen-5-yl)indeno[1,2-*b*]fluorene-6,12-dione (**2OD-TTIFDK**) and 2,2′-(2,8-bis(5′-(2-octyldodecyl)-2,2′-bithiophen-5-yl)indeno[1,2-*b*]fluorene-6,12-diylidene)dimalononitrile (**2OD-TTIFDM**) (Fig. 1). The chemical structures, physicochemical and optoelectronic properties of the new compounds were characterized by ^{1}H/^{13}C NMR, TGA, DSC, UV-vis and CV. Our design yields ultra-low solid-state band gaps of 1.65 eV for **2OD-TTIFDK** and 1.21 eV for **2OD-TTIFDM** with favorable HOMO/LUMO energy levels of $-5.47/-3.61$ eV and $-5.49/-4.23$ eV, respectively, for balanced ambipolarity. Specifically, the sufficiently low LUMO of the dicyanovinylene-functionalized molecule, **2OD-TTIFDM**, enables ambient-stable electron-transport, while the properly aligned HOMO level facilitates hole injection/transport. Top-contact/bottom-gate OFETs fabricated *via* solution-shearing of **2OD-TTIFDM** yield perfectly ambient-stable ambipolar devices with relatively balanced electron and hole mobilities of 0.13 cm^2 V^{-1} s^{-1} and 0.01 cm^2 V^{-1} s^{-1}, respectively, and I_{on}/I_{off} ratios of 10^3–10^4. On the other hand, the carbonyl-functionalized molecule, **2OD-TTIFDK**, exhibits highly balanced

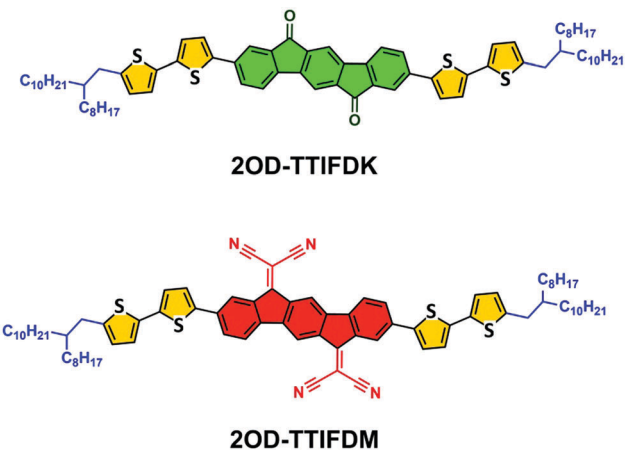

Fig. 1 The chemical structures of **2OD-TTIFDK** and **2OD-TTIFDM** showing the α-substituted bithiophene donor units in yellow, indeno[1,2-*b*]fluorene-6,12-dione (**IFDK**) acceptor unit in green, and indeno[1,2-*b*]fluorene-(6,12-diylidene)dimalononitrile (**IFDM**) acceptor unit in red.

ambipolarity ($\mu_e/\mu_h \sim 2$) under vacuum with electron and hole mobilities of 0.02 $cm^2 V^{-1} s^{-1}$ and 0.01 $cm^2 V^{-1} s^{-1}$, respectively and I_{on}/I_{off} ratios of 10^5–10^6. We have also successfully demonstrated the application of the new ambipolar transistors to complementary-like inverters, which are the building block of integrated circuits for data processing. The new inverters exhibit high voltage gains of 30 under ambient conditions for **2OD-TTIFDM** and 80 under vacuum for **2OD-TTIFDK**. Our findings indicate that although the D–A–D π-skeleton stays the same for both small molecules, energetic stabilization of the LUMO (−3.61 eV → −4.23 eV) as a result of functional group modification is key to the ambient stability of the corresponding OFETs. Theoretical calculations explain the differences in molecular energetics and provide insights into the current functionalization strategies. Our results clearly indicate that the **IFDM** π−core is a proper-sized, favorable acceptor unit for building efficient, soluble ambipolar small molecules to operate under ambient conditions. Considering the processing, charge-transport and inverter characteristics, the current molecular semiconductors are among the best performing ambipolar small molecules in the OFET and CMOS-like inverter literature.

Experimental

Materials and methods

The reagents were purchased from commercial sources and used as received unless otherwise specified. A conventional vacuum/nitrogen manifold system was used, and all the reactions were carried out under N_2. The $^1H/^{13}C$ NMR spectra were recorded on a Bruker 400 spectrometer (^1H, 400 MHz; ^{13}C, 100 MHz), and elemental analyses were performed on a Leco Truspec Micro model instrument. Thermogravimmetric analysis (TGA) and differential scanning calorimetry (DSC) measurements were performed on Perkin Elmer Diamond model instruments under nitrogen at a heating rate of 10 °C min^{-1}. Cyclic voltammetry measurements were performed on a C3 Cell Stand equipped with the Epsilon potentiostat/galvanostat (Bioanalytical Systems, Inc., Lafayette, IN). UV-vis absorption measurements were performed on a UV-vis spectrophotometer (Shimadzu, UV-1800). MALDI-TOF was performed on a BrukerMicroflex LT MALDI-TOF-MS instrument. The total energy minimizations and the optimization of the molecular geometries were carried out using density functional theory (DFT) at the B3LYP/6-31G** level with Gaussian 09.[50] The synthesis of 2-octyldodecylbromide and 2,8-dibromoindeno-[1,2-*b*]fluorene-6,12-dione (**IFDK-Br2**) was conducted in accordance with the reported procedures (see the ESI†).[49]

Synthesis and characterization

Synthesis of 5-(2-octyldodecyl)-2,2′-bithiophene (1). To a solution of 2,2′-bithiophene (1.353 g, 8.14 mmol) in THF (25 mL) at −78 °C was added 3.41 mL (8.52 mmol) of *n*-butyllithium (2.5 M in *n*-hexane) dropwise under nitrogen. The resulting mixture was stirred at −78 °C for 30 min and at room temperature for an additional 1 h. Then, 2-octyldodecylbromide (3.11 g, 8.95 mmol) was added to this mixture slowly at −78 °C. The resulting reaction mixture was stirred at room temperature for 1 h and then heated to 85 °C for 12 h. The reaction was quenched with water, and the product was extracted with chloroform. The organic phase was washed with water, dried over Na_2SO_4, filtered, and evaporated to dryness to yield a crude product, which was purified by column chromatography on silica gel using hexane as the eluent to give the pure product (1.415 g, 38.8% yield). ^1H NMR (400 MHz, $CDCl_3$): δ 0.89 (m, 6H), 1.27–1.35 (m, 33H), 2.72 (d, 2H, J = 6.8 Hz), 6.66 (d, 1H, J = 3.2 Hz), 6.99 (m, 2H), 7.11 (d, 1H, J = 3.2 Hz), 7.17 (d, 1H, J = 5.2 Hz).

Synthesis of trimethyl(5′-(2-octyldodecyl)-[2,2′-bithiophen]-5-yl)stannane (2). To a solution of 5-(2-octyldodecyl)-2,2′-bithiophene (**1**) (1.415 g, 3.17 mmol) in THF (30 mL) at −78 °C was added 1.33 mL (3.33 mmol) of *n*-butyllithium (2.5 M in *n*-hexane) under nitrogen. The mixture was stirred at −78 °C for 30 min and then at room temperature for 1 h. Then, trimethyltin chloride (0.695 g, 3.49 mmol) was added slowly at −78 °C, and the resulting reaction mixture was allowed to warm to room temperature and stirred at room temperature overnight. The reaction was quenched with water, and the product was extracted with hexane. The organic phase was washed with water, dried over Na_2SO_4, filtered, and evaporated to dryness to give the pure product (1.889 g, 97.7% yield). ^1H NMR ($CDCl_3$, 400 MHz): δ 0.39 (s, 9H), 0.89 (m, 6H), 1.27–1.35 (m, 33H), 2.72 (d, 2H, J = 6.4 Hz), 6.65 (d, 1H, J = 3.2 Hz), 6.98 (d, 1H, J = 3.2 Hz), 7.07 (d, 1H, J = 3.6 Hz), 7.22 (d, 1H, J = 3.6 Hz).

Synthesis of 2,8-bis(5′-(2-octyldodecyl)-2,2′-bithiophen-5-yl)-indeno[1,2-*b*]fluorene-6,12-dione (2OD-TTIFDK). The reagents 2,8-dibromo-indeno[1,2-*b*]fluorene-6,12-dione(**IFDK-Br$_2$**) (0.282 g, 0.641 mmol), trimethyl(5′-(2-octyldodecyl)-[2,2′-bithiophen]-5-yl)-stannane (**2**) (0.860 g, 1.41 mmol), and $Pd(PPh_3)_2Cl_2$ (45.0 mg, 0.0641 mmol) in anhydrous DMF (40 mL) were heated at 125 °C under nitrogen for 2 days. Then, the mixture was then cooled to room temperature and quenched with water. The reaction mixture was extracted with chloroform, and the organic phase was washed with water, dried over Na_2SO_4, filtered, and evaporated to dryness to give the crude product. The crude product was then purified by column chromatography on silica gel using chloroform as the eluent to afford the pure product as a dark green solid (0.230 g, 30.6% yield), m.p. 217–218 °C. ^1H NMR (400 MHz, $CDCl_3$): δ 0.90 (m, 6H), 1.28–1.32 (m, 33H), 2.72 (d, 2H, J = 6.4 Hz), 6.64 (d, 1H, J = 3.6 Hz), 6.98 (m, 2H), 7.18 (d, 1H, J = 3.6 Hz), 7.41 (d, 1H, J = 7.6 Hz), 7.62 (d, 1H, J = 8.5 Hz), 7.64 (s, 1H), 7.73 (s, 1H). ^{13}C NMR (100 MHz, $CDCl_3$): δ 14.1, 22.7, 26.6, 29.4, 29.5, 29.6, 29.7, 30.0, 31.9, 33.2, 34.6, 40.0, 115.6, 120.5, 120.8, 123.5, 123.7, 124.4, 125.9, 130.9, 134.4, 134.6, 135.3, 138.2, 139.2, 140.2, 141.3, 144.4, 145.2, 192.1. MS (MALDI-TOF) m/z (M^+): calcd for $C_{76}H_{98}O_2S_4$: 1170.64, found: 1171.74 $[M + H]^+$. Anal. calcd for $C_{76}H_{98}O_2S_4$: C, 77.90; H, 8.43, found: C, 77.98; H, 8.64.

Synthesis of 2,2′-(2,8-bis(5′-(2-octyldodecyl)-2,2′-bithiophen-5-yl)indeno[1,2-*b*]fluorene-6,12-diylidene)dimalononitrile (2OD-TTIFDM). The reagents 2,8-bis(5′-(2-octyldodecyl)-2,2′-bithiophen-5-yl)indeno[1,2-*b*]fluorene-6,12-dione (**2OD-TTIFDKTT**) (0.100 g, 0.085 mmol) and dicyanomethane (79 mg, 1.19 mmol) were dissolved in 12 mL of dry chlorobenzene under nitrogen. Then, pyridine

(0.131 mL, 1.62 mmol) and $TiCl_4$ (0.094 mL, 0.853 mmol) were added and the resulting reaction mixture was heated at 110 °C for 5 h. Then, the reaction was cooled to room temperature and quenched with water. The reaction mixture was extracted with chloroform, and the organic phase was washed with water, dried over Na_2SO_4, filtered, and evaporated to dryness to give the crude product. The crude product was then purified by column chromatography on silica gel using chloroform as the eluent to give the pure product as a dark solid (63 mg, 58.8% yield), m.p. 320–321 °C. ^{1}H NMR (400 MHz, $CDCl_3$): δ 0.90 (m, 6H), 1.27–1.35 (m, 33H), 2.57 (d, 2H, J = 6.0 Hz), 6.50 (d, 1H, J = 3.6 Hz), 6.81 (m, 2H), 7.01 (d, 1H, J = 3.6 Hz), 7.24 (d, 1H, J = 8.0 Hz), 7.42 (d, 1H, J = 8.0 Hz), 8.02 (s, 1H), 8.04 (s, 1H). ^{13}C NMR (100 MHz, $CDCl_3$): δ 14.2, 22.7, 26.5, 29.3, 29.4, 29.6, 29.7, 29.8, 30.0, 32.0, 33.1, 34.5, 39.9, 112.6, 112.7, 117.4, 121.1, 122.3, 123.6, 123.9, 124.8, 126.0, 129.9, 130.2, 134.0, 134.4, 135.4, 138.4, 138.5, 138.9, 139.1, 142.4, 145.0, 158.5. MS (MALDI-TOF) m/z (M^+): calcd for $C_{82}H_{98}N_4S_4$: 1266.67, found: 1267.19 $[M + H]^+$. Anal. calcd for $C_{82}H_{98}N_4S_4$: C, 77.68; H, 7.79; N, 4.42, found: C, 77.96; H, 7.95; N, 4.56.

OFET device fabrication and characterization

All OFETs were fabricated on highly n-doped silicon wafers having a thermally oxidized 300 nm SiO_2 dielectric (capacitance per unit area C_i = 11.4 nF cm^{-2}) by adopting the top-contact/bottom-gate (TC/BG) device architecture. The substrates were cleaned *via* sonication in acetone for 10 min followed by oxygen plasma cleaning for 5 min (Harrick plasma, PDC-32G, 18 W). The PS (polystyrene)-brush treatment was performed in accordance with the reported procedures (M_w = 1.7–10 kg mol^{-1}) to achieve favorable dielectric–semiconductor interfaces.[51–53] The organic semiconductor layers (**2OD-TTIFDK** and **2OD-TTIFDM**) were deposited *via* a solution-shearing method on PS-brush-treated substrates. The solution-shearing method was performed based on the reported procedure, and the conditions were optimized with respect to the solvent, concentration of solution, temperature of substrate, shearing speed, and thermal annealing temperature.[54] The solution-sheared substrates were kept in a vacuum oven at 150 °C for 30 min, and then placed in a desiccator for 24 h to remove the residual solvent. A profilometer (DEKTAK-XT, Brucker) was used to measure the OSC film thicknesses (30–60 nm). The top electrodes were thermally evaporated (deposition rate = 0.2 Å s^{-1}) as Au layers (50 nm) with various channel widths (W; 1000 and 500 μm) and lengths (L; 100 and 50 μm). A Keithley 4200-SCS was used to characterize the electronic performances of the OFETs under ambient conditions or in a vacuum probe station ($<10^{-2}$ Torr) at room temperature. The electronic performance in the saturation region such as charge carrier mobilities (μ) and threshold voltages (V_T) were extracted from the equation:

$$\mu_{sat} = (2I_{DS}L)/[WC_i(V_G - V_T)^2]$$

where I_{DS} is the drain current, L and W are the channel length and width, respectively, C_i is the areal capacitance of the gate dielectric, V_G is the gate voltage, and V_T is the threshold voltage. The reported OFET characteristics are the average of 10 different devices with standard deviations of less than 5–10%. The surface morphology and microstructure of thin-films were measured by atomic force microscopy (AFM, NX10, Park systems) and X-ray diffraction (XRD, Smartlab, Rigaku), respectively.

Fabrication and characterization of complementary-like inverters

The complementary-like inverters were fabricated on the PS-brush treated n^{++}-Si/SiO_2 gate-dielectric substrate using two identical ambipolar OFETs based on **2OD-TTIFDK** or **2OD-TTIFDM** with a common gate as the input voltage (V_{IN}). The top electrodes with various channel widths (W; 2000, 1000, and 500 μm) and lengths (L; 100 and 50 μm) were deposited through a shadow mask to define the electrode of supply bias (V_{DD}), the common electrode of output voltage (V_{OUT}), and the ground electrode. The channel dimensions for the two ambipolar OFETs were identical. The complementary-like inverters were characterized with the Keithley 4200-SCS instrument under ambient conditions or under vacuum ($<10^{-2}$ Torr).

Results and discussion

Computational modeling, synthesis and characterizations

A density-functional theory (DFT) study was performed on the model compounds **M1** and **M2** prior to the synthesis to gain initial insights into the molecular and electronic structures of the new molecules (Fig. 2). In these model compounds, shorter chains (isobutyl) were employed instead of longer alkyl chains (2-octyldodecyl) to ease the calculations by reducing the degrees of freedom. Based on the energy-minimized geometries, **IFDK** and **IFDM** π–cores are found to adopt high co-planarity, while some degree of acceptable inter-ring twist exists between these cores and outer thiophene units ($\theta < 22°$). For both compounds, the HOMO is highly delocalized along the molecular backbone and the LUMO is more localized on the acceptor cores. However, the proper size of the acceptor unit may still ensure efficient intra-/inter-molecular π-delocalization and therefore good electron transport. The theoretical HOMO–LUMO energy gaps are estimated as 2.27 eV for **M1** and 1.45 eV for **M2**. The large reduction in the energy gap originates mainly from the LUMO level reduction (−2.90 eV → −3.87 eV) as a result of functional group modification from carbonyl to dicyanovinylene. The origin of this reduction is a result of favorable inductive and mesomeric effects of dicyanovinylene *vs.* carbonyl ensuring very low LUMO levels with minimal influences on the HOMO energy level. The low LUMO energy level of **M2** is ideal for air-stable electron transport, which, when combined with its still relatively high HOMO, should enable ambipolarity under ambient conditions. It is noteworthy that although ambipolarity may also be expected from **M1**, based on its relatively high LUMO, electron-transport is not expected to be stable under ambient conditions.

Scheme 1 shows the synthesis of the stannylated π–donor moiety, trimethyl(5′-(2-octyldodecyl)-[2,2′-bithiophen]-5-yl)stannane (**2**) and the corresponding α,ω-disubstituted molecules **2OD-TTIFDK** and **2OD-TTIFDM**. The synthesis of the ladder-type acceptor core **IFDK-Br2** was carried out *via* Suzuki cross-coupling

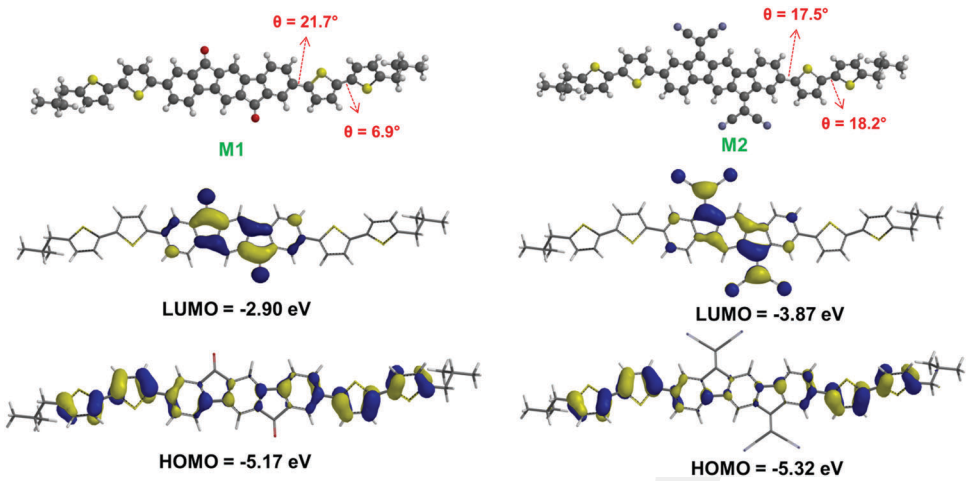

Fig. 2 Chemical structures of the model compounds **M1** and **M2**. Optimized molecular geometries showing inter-ring dihedral angles, computed HOMO and LUMO energy levels, and topographical orbital representations (DFT, B3LYP/6-31G**).

and intramolecular Friedel–Crafts acylation reactions in accordance with the established procedure by our group (Scheme S1, ESI†). The donor unit, **2**, was prepared from bithiophene in two steps: in the first step, bithiophene was monolithiated and capped with 2-octyldodecylbromide to yield **1** in 39% yield, and subsequently, **2** was synthesized from **1** in 98% yield *via* a conventional lithiation/stannylation reaction. The synthesis of the new carbonyl functionalized ladder type compound **2OD-TTIFDK** was carried out *via* conventional Stille cross-coupling reaction by reacting **IFDK-Br2** and **2** in DMF using a $Pd(PPh_3)_2Cl_2$ catalyst in 31% yield. Since the solubility of **IFDK-Br2** was very low in common organic solvents, the success of this reaction relies on using a highly polar solvent (DMF) at high temperature (125 °C). During the course of this reaction, the coupling of the first π–donor moiety having a 2-OD chain enhances the solubility of the mono-coupled adduct significantly so that the second coupling proceeds more easily. A dicyanovinylene functionalized molecule, **2OD-TTIFDM**, was synthesized *via* Knoevenagel condensation between **2OD-TTIFDK** and malononitrile in the presence of pyridine and $TiCl_4$ in 59% yield. Thanks to the presence of swallow-tailed 2-OD alkyl substituents, the new D–A–D molecules are found to be very soluble in common organic solvents ($CHCl_3$, THF, Toluene, *etc.*) and purifications were performed by flash column chromatography using silica gel and chloroform as the stationary phase and eluent, respectively. The good solubilites of the new molecules also enable the fabrication of OFETs *via* solution-processing. The chemical structures and purities of the intermediate and final products were confirmed by $^1H/^{13}C$ NMR (Fig. S1–S5, ESI†), mass spectroscopy (MALDI-TOF) (Fig. S3 and S6, ESI†), elemental analysis, and ATR-FTIR (Fig. S7, ESI†). Based on thermogravimetric analysis (TGA), both compounds exhibited good thermal stabilities with onset decomposition temperatures over 350 °C (Fig. S8A, ESI†). Differential scanning calorimetry (DSC) measurements of **2OD-TTIFDK** and **2OD-TTIFDM** exhibited high-temperature endotherms at 218 °C and 320 °C, respectively, which are in accordance with the conventional melting temperature measurements (Fig. S8B, ESI†). Surprisingly, higher-energy endothermic thermal transitions (179/208 °C for **2OD-TTIFDK** and 209 °C for **2OD-TTIFDM**) were observed for both compounds prior to the major melting process, which are typical characteristics of

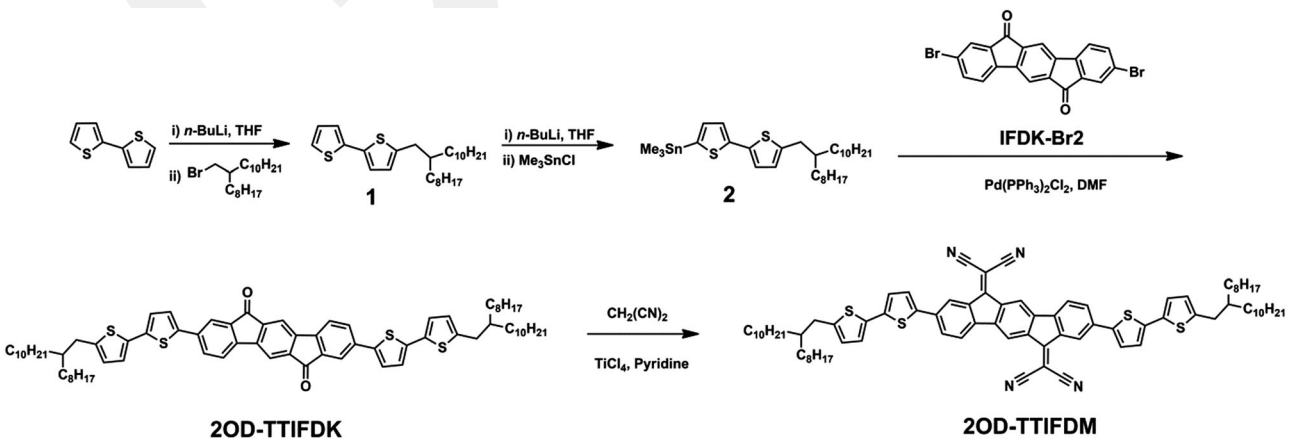

Scheme 1 Synthesis of **2OD-TTIFDK** and **2OD-TTIFDM**.

liquid-crystalline materials.[55] Upon cooling, the DSC traces of both compounds displayed the same behavior of their heating cycle. Although the π-skeleton remains the same for both compounds, the melting temperature significantly increases (ΔT_m = +102 °C) when the functional group is changed from carbonyl ("C=O" in **2OD-TTIFDK**) to dicyanovinylene ("C=C(CN)$_2$" in **2OD-TTIFDM**). This indicates more effective cohesive forces in the solid-state packing for the latter molecule, which is likely a combined result of larger local/molecular dipole moments and enhanced dipole–dipole/π–π interactions as a result of stronger donor–acceptor characteristics. When compared with our previously reported compound, **2OD-TIFDKT** (Fig. S9, ESI†),[49] the introduction of additional thiophenes at molecular termini significantly increased T_m by ~80 °C in **2OD-TTIFDK** as a result of enhanced π–core rigidity.

As shown in Fig. 3, when the concentrations of **2OD-TTIFDK** and **2OD-TTIFDM** in $CDCl_3$ increased from 1.0 mg mL^{-1} to 16.0 mg mL^{-1}, the chemical shifts of the aromatic and α-aliphatic protons moved upfield ($-\Delta\delta$ = 0.1–0.4 ppm), indicating the presence of a shielding effect. This shielding is due to enhanced electron-density on individual protons as a result of molecular stacking in organic solvents *via* intermolecular π–π stacking and van der Waals interactions. The aromatic protons that show chemical shifts originated both from **IFDK/IFDM** π–cores and bithiophene units, as well as the *alpha*-methylene proton (Ar-C**H$_2$**-CH(C_8H_{17})$C_{10}H_{21}$) adjacent to the thiophenes, indicating that all these protons are involved in the intermolecular interactions in the molecular stacks. The aromatic peaks were broadened with increasing concentration, which further supports the stacking model since intermolecular attractions widen the local electronic profile around each proton. Similar stacking behaviors were observed for a number of π-conjugated small molecules in the literature.[56–58] This indicates the existence of favorable intermolecular interactions for the present D–A–D π–cores even in the solution-phase, which may potentially render the formation of favorable supramolecular architecture after solvent removal in the solid-state (*vide infra*).

Optical and electrochemical properties

The UV-vis absorption spectra (Fig. 4A) of **2OD-TTIFDK** and **2OD-TTIFDM** in dichloromethane solutions exhibit similar higher energy maxima at 410 nm and 400 nm, respectively, corresponding to the π–π* transitions of the bithiophene-indeno[1,2-*b*]fluorene core, which remain the same for both compounds although the functional groups are different. However, lower-energy peaks appear at 568 nm and 740 nm for **2OD-TTIFDK** and **2OD-TTIFDM**, respectively, reflecting the differences in the chemical nature of carbonyl *vs.* dicyanovinylene functional groups. Therefore, these relatively weaker lower-energy transitions are most likely to be governed by the functional groups and originate from symmetry forbidden n–π* transitions.[59,60] The optical band gaps in solution are calculated from the low-energy absorption edges as 1.89 eV (**2OD-TTIFDK**) and 1.31 eV (**2OD-TTIFDKM**). Both compounds exhibit significant bathochromic shifts ($\Delta\lambda$ = 16–216 nm) and reductions in optical band gaps when going from dilute solution to the solid-state (Fig. 4B). This is indicative of molecular planarization and enhanced π–π stacking/donor–acceptor interactions in the solid-state. The solid-state optical band gaps are estimated at 1.65 eV for **2OD-TTIFDK** and 1.21 eV for **2OD-TTIFDM**, which are, to the best of our knowledge, among the lowest in the literature for π-conjugated small molecules. It is noteworthy that the optical band-gap and absorption maxima observed for the present compound, **2OD-TTIFDM**, is ~0.15 eV smaller and ~30 nm red-shifted, respectively, compared to those of structurally related compound, **β-C12-TTIFDM** (1.44 eV; λ_{max} = 410, 711 nm).[48] This is due to repositioning of the hydrocarbon chains from β- to α,ω-positions (Fig. S9, ESI†) in the new semiconductor, which minimizes the inter-ring twists between donor and acceptor units (θ_{Ph-Th} = 45–46° → 16–17°) and further extends the π-conjugation on the present compound. This is found to be very advantageous to the charge carrier mobilities in the corresponding OFET devices (*vide infra*).

As shown in Fig. 4C, cyclic voltammetry (CV) measurements of **2OD-TTIFDK** and **2OD-TTIFDM** in dichloromethane solutions exhibit reversible oxidation and reduction peaks with the first half-wave potentials located at 1.07 V/−0.79 V (*vs.* Ag/AgCl) and

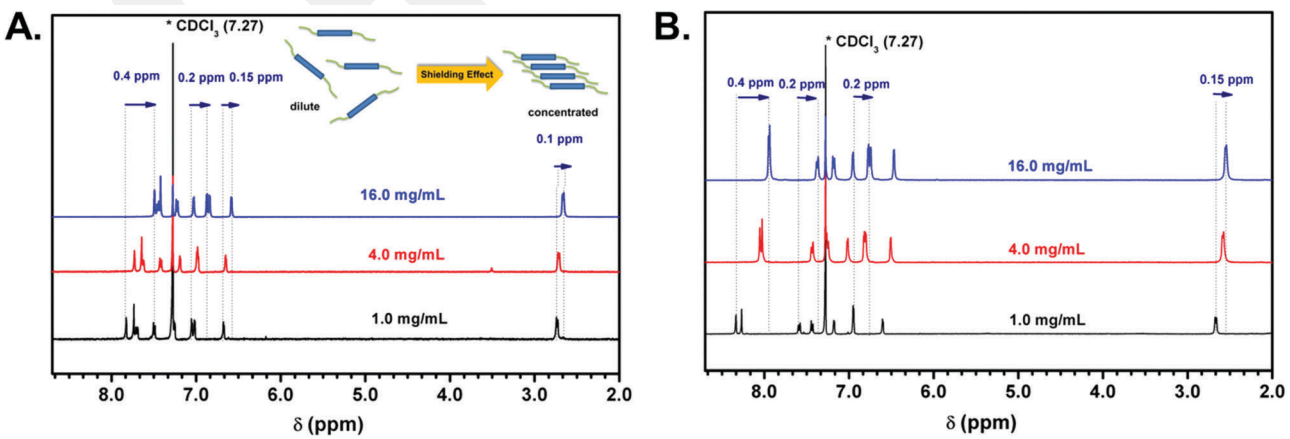

Fig. 3 The concentration dependent ^{1}H NMR spectra of **2OD-TTIFDK** (A) and **2OD-TTIFDM** (B) in $CDCl_3$. Inset is the schematic model of molecular stacking in solution as a result of concentration. (The blue and green units represent π-backbone and flexible hydrocarbon chains, respectively.)

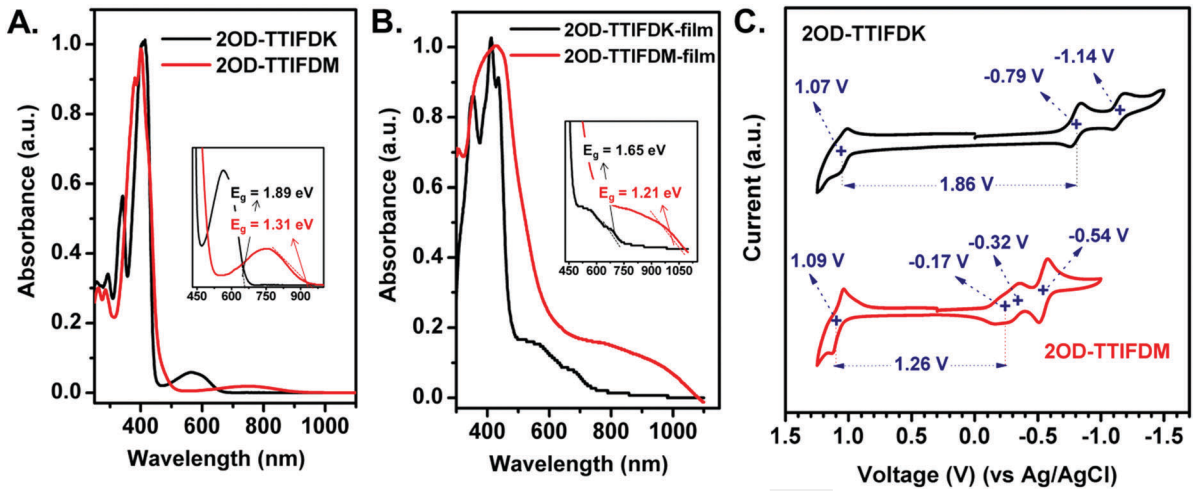

Fig. 4 For compounds **2OD-TTIFDK** and **2OD-TTIFDM**, (A) optical absorption in dichloromethane solution, (B) optical absorption as thin-films, and (C) cyclic voltammograms in dichloromethane (0.1 M $Bu_4N^+PF_6^-$, scan rate = 50 mV s^{-1}.) The insets in A and B show the low-energy absorption onsets and the calculated optical band gaps.

1.09 V/−0.17 V (*vs.* Ag/AgCl), respectively. The existence of both oxidative and reductive electrochemical processes with good reversibility indicates the intrinsic redox-stable ambipolar nature of the present compounds. Due to the stronger electron accepting nature of dicyanovinylene in **2OD-TTIFDM** compared to carbonyl in **2OD-TTIFDK**, the reduction potential shows significant anodic shift (−0.79 V → −0.17 V) with minimal impact on the oxidation potentials. The corresponding HOMO/LUMO energy levels are estimated as −5.47 eV/−3.61 eV for **2OD-TTIFDK** and −5.49 eV/−4.23 eV for **2OD-TTIFDM**, using the vacuum level energy of Ag/AgCl as −4.40 eV. These observations are consistent with our theoretical findings (*vide supra*) that for both compounds, the HOMOs are delocalized along the same molecular backbone and the LUMOs are localized on the acceptor core functionalities. On the basis of the oxidation and reduction potentials, the electrochemical band gaps for **2OD-TTIFDK** and **2OD-TTIFDM** are estimated as 1.86 eV and 1.26 eV, respectively, which are in perfect agreement with the optical band gaps. Based on the molecular orbital energetics and low band gaps, the HOMO (−5.47 to −5.49 eV) and LUMO (−3.61 to −4.23 eV) energies of the current compounds should favor concurrent electron and hole injection/transport (ambipolarity) in the corresponding thin-films. Specifically, the LUMO level of **2OD-TTIFDM** is highly favorable for ambient-stable electron-transport.

Field-effect transistor and complementary-like inverter fabrication and characterization

Top-contact/bottom-gate (TC/BG) OFETs were fabricated by solution-shearing 30–60 nm thick films of **2OD-TTIFDK** and **2OD-TTIFDM** on PS-brush treated n^{++}-Si/SiO_2 (300 nm) substrates to achieve favorable semiconductor–dielectric interfaces with higher semiconductor film quality and better control on the microstructure/morphology, as compared to conventional solution-based methods such as drop casting and spin coating.[61,62] For both semiconductors, the most ideal solution-shearing condition was identified as applying 1.0 mg mL^{-1} (in chlorobenzene) semiconductor formulations on substrates maintained at 50–60 °C at a shearing speed of ~1.0 mm min^{-1}. OFET devices were characterized under positive and negative gate biases under ambient conditions and under vacuum to explore the ambipolarity, device performance, and ambient stability. Typical transfer and output curves are shown in Fig. 5 and Fig. S10–S13 (ESI†), and the corresponding OFET data are summarized in Table 1.

As expected from the optical/electrochemical and theoretical characterizations (*vide supra*), all OFET devices fabricated with the current semiconductors, **2OD-TTIFDM** and **2OD-TTIFDK**, were found to exhibit typical ambipolar characteristics. This indicates the intrinsic ambipolar semiconducting nature of the present compounds and can be attributed to their low solid-state band gaps (1.21–1.65 eV), which render both the HOMO and LUMO levels energetically accessible for hole and electron injection/transport, respectively. Consistent with its highly stabilized LUMO energy level of −4.23 eV, **2OD-TTIFDM** is found to be perfectly ambient-stable as a semiconductor thin-film in OFETs with electron and hole mobilities of 0.13 $cm^2 V^{-1} s^{-1}$ and 0.01 $cm^2 V^{-1} s^{-1}$, respectively, and I_{on}/I_{off} ratios of ~10^3–10^4 under ambient conditions (Fig. 5). These devices are found to exhibit negligible variations in transistor characteristics after a few months of storage under ambient conditions, showing the prolonged stability of the corresponding semiconductor thin-films (Fig. S12, ESI†). When the semiconductor performance of **2OD-TTIFDM** is compared with that of structurally related **β-C12-TTIFDM**[48] (Fig. S9, ESI†), which includes additional linear alkyl chains at thiophenes' β-positions, two orders of magnitude (×100) higher electron (μ_e = 1 × 10^{-3} $cm^2 V^{-1} s^{-1}$ → 0.13 $cm^2 V^{-1} s^{-1}$) and hole (μ_h = 1 × 10^{-4} $cm^2 V^{-1} s^{-1}$ → 0.01 $cm^2 V^{-1} s^{-1}$) mobilities were achieved with the current semiconductor, **2OD-TTIFDM**. The substantial mobility improvements observed for the new semiconductor probably reflects a combination of D–A–D π–core planarization as a result of reducing inter-ring D–A twists (*vide supra*) and improved thin-film microstructure/morphology due to the solution-shearing process.

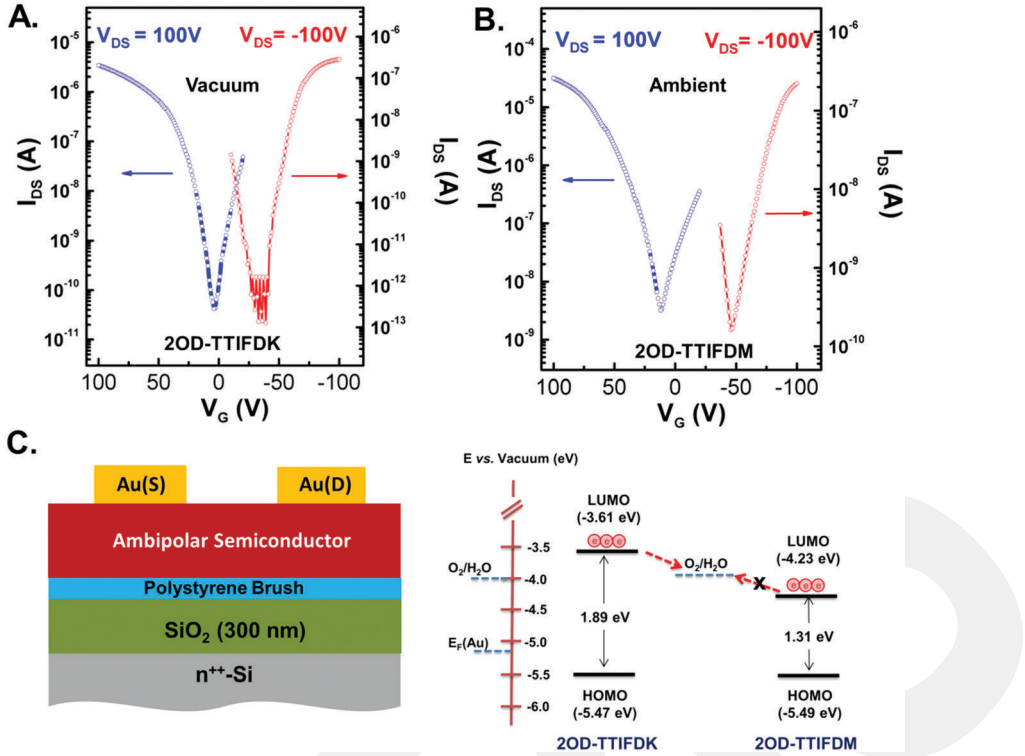

Fig. 5 (A and B) Ambipolar (p-channel (in red) and n-channel (in blue)) transfer curves of the OFET devices based on solution-sheared thin-films of **2OD-TTIFDK** and **2OD-TTIFDM**, and (C) top-contact/bottom-gate OFET device structure and the band lineups of the molecular orbital energy levels with respect to the O_2/H_2O electrochemical redox couple at the air–thin film interface.

Table 1 Electrical performance of OFETs based on **2OD-TTIFDK** and **2OD-TTIFDM** developed in this study[a]

	n-Channel			p-Channel		
Material	μ_e ($cm^2\ V^{-1}\ s^{-1}$)	V_T (V)	I_{on}/I_{off}	μ_h ($cm^2\ V^{-1}\ s^{-1}$)	V_T (V)	I_{on}/I_{off}
2OD-TTIFDK	0.02 ± 0.002	34 ± 3	1.4×10^5	0.01 ± 0.001	−55 ± 4	2.2×10^6
2OD-TTIFDM	0.13 ± 0.012	13 ± 2	1.0×10^4	0.01 ± 0.002	−33 ± 2	1.1×10^3

[a] The OFETs based on **2OD-TTIFDK** and **2OD-TTIFDM** were measured under vacuum and under ambient conditions, respectively.

From a structural design standpoint, in the development of ambipolar small molecules employing donor–acceptor linkages, we can suggest that it's important to minimize the inter-ring twists between donor and acceptor units. On the other hand, due to its relatively higher LUMO energy level of −3.61 eV, OFETs fabricated with **2OD-TTIFDK** were only active under vacuum; they exhibit a highly balanced ($\mu_e/\mu_h \sim 2$) ambipolar behavior with mobilities of 0.02 $cm^2\ V^{-1}\ s^{-1}$ (for n-channel) and 0.01 $cm^2\ V^{-1}\ s^{-1}$ (for p-channel) with $I_{on/off}$ ratios of $\sim 10^5$–10^6, respectively. When **2OD-TTIFDK**-based OFETs were measured in ambient conditions, although the p-channel performance remained at the same level, the n-channel performance showed a significant initial drop (×100) and eventually became inactive (Fig. S13, ESI†). The transition of electron transport from being unstable to ambient-stable was clearly observed for the present semiconductors when the functional group was changed from carbonyl to dicyanovinylene, even though the π-backbone (bithiophene-indeno[1,2-*b*]fluorene-bithiophene) remains the same. This indicates the importance of molecular orbital energetics stabilization for ambient-stable electron-transport in semiconductor thin-films and an electrochemical threshold exists between −3.6 eV and −4.2 eV. This is consistent with earlier reports, and corresponds to a required stabilization of the LUMO energy level against electrochemical trapping by the O_2–H_2O redox couple.[48,63] To the best of our knowledge, the OFET characteristics of **2OD-TTIFDM** are among the best solution-processed, small molecular ambipolar performances in terms of reasonably balanced and ambient-stable charge carrier mobilities. It's noteworthy that further device structure optimizations such as using ferroelectric dielectrics[20] and adding graphene oxide (GO)[64] or single-walled carbon nanotube (SWNT)[65] interlayers can be employed to further balance the electrical characteristics of hole- *vs.* electron-transport with the current ambipolar semiconductors.

Complementary-like inverters are an essential building block of integrated circuits for data processing, and they typically require the fabrication of separate p- and n-channel transistors. However, when an ambipolar semiconducting material is used, only a single layer of organic semiconductor is required without

the need for separate patterning of unipolar p- and n-channel semiconductors. Therefore, given the promising high-performance, well-balanced ambipolar OFET characteristics of the new semiconductors, complementary-like inverters were fabricated from **2OD-TTIFDK** or **2OD-TTIFDM** semiconductor solutions and characterized on single substrates using two identical ambipolar transistors with a shared gold electrode (Fig. 6-inset). As shown in Fig. 6 and Fig. S14 (ESI†), complementary-like inverters based on **2OD-TTIFDK** and **2OD-TTIFDM** operated well under vacuum and under ambient conditions, respectively, in the first and third quadrants with sharp switchings of V_{OUT}'s at supplied voltages (V_{DD}) of +100 and −100 V, respectively. The voltage gain is calculated from $|dV_{OUT}/dV_{IN}|$, where V_{OUT} and V_{IN} are the output and input voltages, respectively. The ability of the current inverters to operate in both quadrants is the specific advantage of having ambipolar OFETs.[66,67] For **2OD-TTIFDK**-based inverters, a very high voltage gain of 80 V/V was achieved at positive V_{IN} along with a maximum gain of 28 V/V at negative V_{IN}. To the best of our knowledge, the high voltage gain in the first quadrant is among the highest voltage gains achieved with a solution-processed, single-component ambipolar semiconductor.[68–70] High voltage gain from sharp voltage inversion demonstrates the reliability of the current inverter devices, and can be attributed to the highly balanced ambipolar charge-transport behavior of **2OD-TTIFDK** (*vide supra*).[71] On the other hand, inverters based on an ambient-stable semiconductor, **2OD-TTIFDM**, were characterized under ambient conditions, and they exhibited good voltage gains of 30 V/V (Fig. S14, ESI†). Our results show that the current solution-processable ambipolar small molecules are ideal semiconductors not only for ambipolar OFETs but also for single-component CMOS-like organic circuits. However, it's noteworthy that the observed Z-shaped voltage transfer characteristics (*VTC*) for both semiconductors are typical for unoptimized ambipolar transistor-based inverters, since both the pull-up (p-channel) and pull-down (n-channel) transistors cannot be completely switched off at low and high V_{IN}'s.[64] These features will cause limited noise margin and large static power consumption, and further inverter device optimizations such as semiconductor film doping or incorporating interlayers are needed to further match charge carrier mobilities (μ) and threshold voltages (V_T) in the p- and n-channel regions.[65]

Thin-film microstructure and morphology

The microstructural and morphological characteristics of the solution-sheared thin-films of the current semiconductors were investigated using an out-of-plane $\theta-2\theta$ X-ray diffraction (XRD) technique and atomic force microscopy (AFM). As shown in Fig. 7, both semiconductor thin-films showed crystalline patterns with distinct (00*l*) diffraction peaks up to the third order along with broad (0*k*0) peaks. The primary diffraction peaks (001) were observed at $2\theta = 3.05^\circ$ (*d*-spacing = 29.0 Å) for **2OD-TTIFDK** and at $2\theta = 2.37^\circ$ (*d*-spacing = 37.2 Å) for **2OD-TTIFDM**, indicative of the formation of well-organized lamellar microstructure having molecular/alkyl-chain edge-on orientation relative to the dielectric surface. Further weak diffraction peaks were observed at $2\theta = 4.24^\circ$ (001′) and 5.34° (001″) for **2OD-TTIFDK**-based thin-film, which do not belong to the primary diffraction family, indicating the existence of additional minor crystalline phases.

The *d*-spacings for both compounds are shorter than the computed molecular lengths (~57.0 Å) with fully extended (all-trans conformation) alkyl chains. This indicates that significant alkyl chain interdigitation and/or molecular tilting from the substrate normal are likely to occur in thin-film phases. Considering that the alkyl chains remain the same for both semiconductors, the larger *d*-spacing observed for **2OD-TTIFDM** reflects more vertically oriented molecular π–cores relative to the dielectric surface, probably as a result of stronger intermolecular interactions between D–A–D π–cores (*vide supra*). The **2OD-TTIFDM** thin-film exhibited a much stronger (001) diffraction peak intensity (×7 for the same film thickness) with smaller FWHM (full width at half maximum) (~0.20° *vs.* ~0.35°) when compared with that of **2OD-TTIFDK**. This shows that **2OD-TTIFDM** thin-films have higher crystallinity with a larger mean crystallite size.[72] Broad diffraction peaks observed at $2\theta \sim 22^\circ$ (010) were ascribed to π–π stacking interactions with distances of ~4.1 Å between

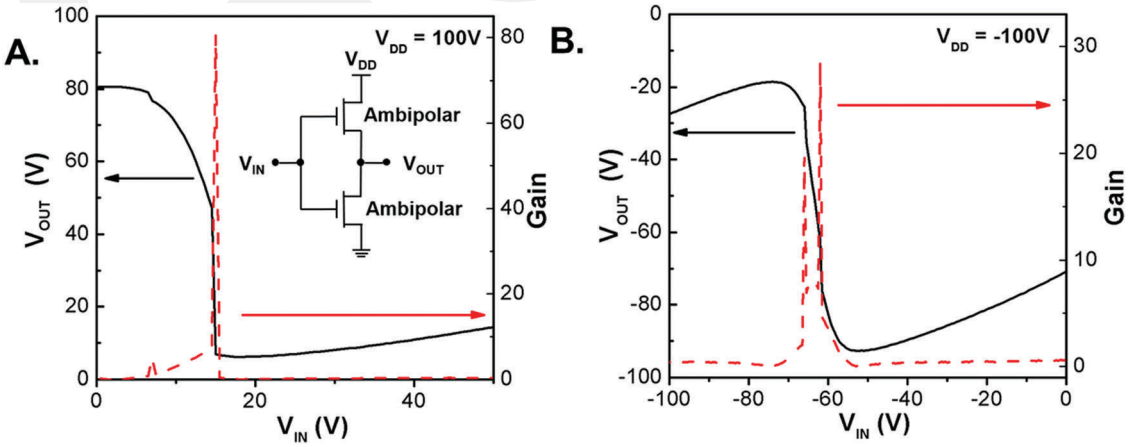

Fig. 6 Voltage transfer characteristics (VTC) of a complementary-like inverter fabricated by two identical **2OD-TTIFDK**-based ambipolar transistors in the first (A) and third (B) quadrants with supplied voltages of +100 V and −100 V. Inset shows the circuit diagram and the plots of gains ($-dV_{OUT}/dV_{IN}$) are given in red.

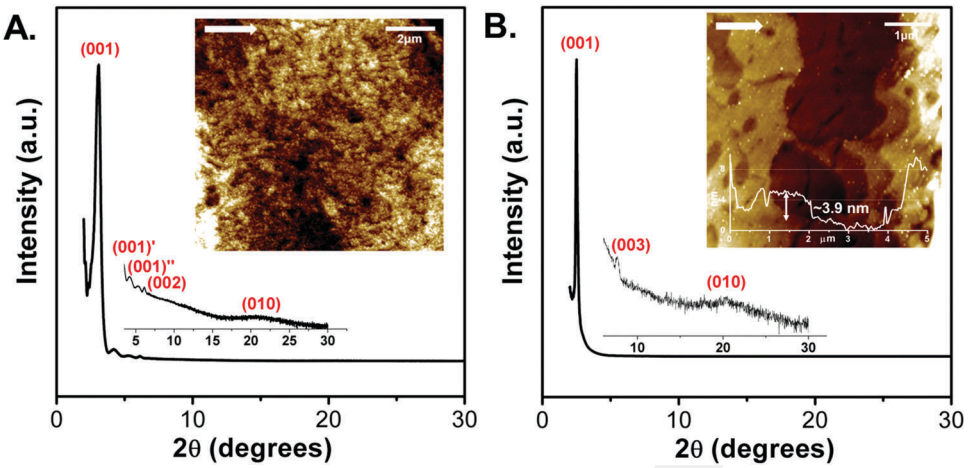

Fig. 7 θ–2θ X-ray diffraction (XRD) scans and AFM topographic images (inset) of **2OD-TTIFDK** (A) and **2OD-TTIFDM** (B) thin-films fabricated by the solution shearing method. The scale bar denotes 1–2 μm and the arrow shows the shearing direction.

molecular backbones, which is somewhat larger than the typical π–π stackings observed for oligo-/polythiophenes (3.4–3.9 Å).[48,73,74] This points to the relatively weaker π–π stacking interactions for the current semiconductors and it can be attributed to the presence of sterically bulky, swallow-tailed 2-octyldodecyl substituents, which may preclude the π–cores from approaching each other effectively. AFM characterizations provide more information on the morphological aspects of the current films, and, therefore, allow us to better understand the correlations with the electrical performances. Both films reveal highly homogeneous morphologies with surface roughness below 4–5 nm for 10 × 10 μm scan areas. Although the **2OD-TTIFDK** films exhibited small highly-interconnected isotropic spherulites (~100–200 nm diameter sizes), the **2OD-TTIFDM** films revealed two-dimensional micron-size (~1–2 μm) plate-like grains of terraced islands with step-heights of ~3.9 nm, which correspond to the *d*-spacing measured from the XRD characterization (~3.7 nm). The observed highly crystalline and edge-on π-oriented microstructure, and layer-by-layer grown 2-D morphology of the **2OD-TTIFDM** film favors efficient charge-transport in OFETs. Furthermore, when these favorable microstructural/morphological features are compared with those of the **2OD-TTIFDK**-based thin-film, it seems to significantly enhance the field-effect electron mobility (×6) with minimal influence on the field-effect hole mobility. This shows that thin-film morphological and microstructural characteristics may have totally different effects on the electron and hole charge-transport characteristics of molecular solids.

Conclusions

Two new solution-processable ambipolar small molecules, **2OD-TTIFDK** and **2OD-TTIFDM**, have been designed, synthesized and fully characterized. The new semiconductors having strong D–A–D π-architectures employ ladder-type π–acceptors of **IFDK/IFDM** and α-substituted bithiophene π–donors, which results in ultralow band gaps of 1.21–1.65 eV. The HOMO/LUMO frontier orbital energies of the new molecules (−5.47/−3.61 eV for **2OD-TTIFDK** and −5.49/−4.23eV for **2OD-TTIFDM**) are found to be highly favorable for balanced ambipolar charge-transport and ambient-stability for **2OD-TTIFDM**. The resulting bottom-gate/top-contact OFET devices fabricated by solution-shearing **2OD-TTIFDM** show clear ambipolar characteristics under ambient conditions with reasonably balanced carrier mobilites of 0.13 $cm^2\ V^{-1}\ s^{-1}$ for electrons and 0.01 $cm^2\ V^{-1}\ s^{-1}$ for holes with I_{on}/I_{off} ratios of $\sim 10^3$–10^4. **2OD-TTIFDK**-based OFETs exhibit ambipolarity under vacuum with highly balanced ($\mu_e/\mu_h \sim 2$) electron and hole mobilities of 0.02 $cm^2\ V^{-1}\ s^{-1}$ and 0.01 $cm^2\ V^{-1}\ s^{-1}$, respectively with I_{on}/I_{off} ratios of $\sim 10^5$–10^6. Most importantly, complementary-like inverters were demonstrated based on the new ambipolar small molecules, which showed sharp signal switching with very high gains of up to 80. When the charge transport stabilities of the current semiconductors are compared, our observations show that the ambient-stability of charge-transport in ambipolar semiconductors is governed mainly by the stabilization of conducting electrons in the LUMO energy level. To the best of our knowledge, the current D–A–D π-structures are among the best performing ambipolar small molecules for OFET and complementary-like inverter devices. Our findings clearly provide an efficient approach for the preparation of ultralow band-gap small molecules as ambient-stable and solution-processable ambipolar semiconductors for various organic optoelectronic technologies including CMOS-like integrated circuits.

Acknowledgements

H. U. and R. O. acknowledges support from AGU-BAP (FYL-2016-65). H. U. acknowledges support from Turkish Academy of Sciences, The Young Scientists Award Program (TUBA-GEBIP 2015) and The Science Academy, Young Scientist Award Program (BAGEP 2014). C. K. acknowledges support from Development of Space Core Program (2016M1A3A3A02016885) and Basic Science Research Program through the National Research Foundation of Korea (NRF) (NRF-2014R1A1A1A05002158).

References

1 K. Zhou, H. Dong, H.-L. Zhang and W. Hu, *Phys. Chem. Chem. Phys.*, 2014, **16**, 22448–22457.
2 H. Usta, W. C. Sheets, M. Denti, G. Generali, R. Capelli, S. Lu, X. Yu, M. Muccini and A. Facchetti, *Chem. Mater.*, 2014, **26**, 6542–6556.
3 J. Zaumseil, R. H. Friend and H. Sirringhaus, *Nat. Mater.*, 2006, **5**, 69–74.
4 R. Capelli, S. Toffanin, G. Generali, H. Usta, A. Facchetti and M. Muccini, *Nat. Mater.*, 2010, **9**, 496–503.
5 M. Durso, C. Bettini, A. Zanelli, M. Gazzano, M. G. Lobello, F. De Angelis, V. Biondo, D. Gentili, R. Capelli and M. Cavallini, *et al.*, *Org. Electron.*, 2013, **14**, 3089–3097.
6 J. Lee, M. Jang, S. Myeon Lee, D. Yoo, T. J. Shin, J. H. Oh and C. Yang, *ACS Appl. Mater. Interfaces*, 2014, **6**, 20390–20399.
7 A. D. Scaccabarozzi and N. Stingelin, *J. Mater. Chem. A*, 2014, **2**, 10818.
8 S. C. Martens, U. Zschieschang, H. Wadepohl, H. Klauk and L. H. Gade, *Chem. – Eur. J.*, 2012, **18**, 3498–3509.
9 L. Chua, J. Zaumseil, J. Chang, E. C.-W. Ou, P. K.-H. Ho, H. Sirringhaus and R. H. Friend, *Nature*, 2005, **434**, 194–199.
10 K. J. Baeg, J. Kim, D. Khim, M. Caironi, D. Y. Kim, I. K. You, J. R. Quinn, A. Facchetti and Y. Y. Noh, *ACS Appl. Mater. Interfaces*, 2011, **3**, 3205–3214.
11 C. Rost, D. J. Gundlach, S. Karg and W. Rieß, *J. Appl. Phys.*, 2004, **95**, 5782–5787.
12 J. Cornil, J.-L. Brédas, J. Zaumseil and H. Sirringhaus, *Adv. Mater.*, 2007, **19**, 1791–1799.
13 X. Xu, T. Xiao, X. Gu, X. Yang, S. V. Kershaw, N. Zhao, J. Xu and Q. Miao, *ACS Appl. Mater. Interfaces*, 2015, **7**, 28019–28026.
14 S. S. Cheng, P. Y. Huang, M. Ramesh, H. C. Chang, L. M. Chen, C. M. Yeh, C. L. Fung, M. C. Wu, C. C. Liu and C. Kim, *et al.*, *Adv. Funct. Mater.*, 2014, **24**, 2057–2063.
15 J. Zaumseil and H. Sirringhaus, *Chem. Rev.*, 2007, **107**, 1296–1323.
16 R. P. Ortiz, H. Herrera, C. Seoane, J. L. Segura, A. Facchetti and T. J. Marks, *Chem. – Eur. J.*, 2012, **18**, 532–543.
17 A. Riaño, P. Mayorga Burrezo, M. J. Mancheño, A. Timalsina, J. Smith, A. Facchetti, T. J. Marks, J. T. López Navarrete, J. L. Segura and J. Casado, *et al.*, *J. Mater. Chem. C*, 2014, **2**, 6376–6386.
18 J. Lee, A. R. Han, H. Yu, T. J. Shin, C. Yang and J. H. Oh, *J. Am. Chem. Soc.*, 2013, **135**, 9540–9547.
19 J. Li, Y. Zhao, H. S. Tan, Y. Guo, C.-A. Di, G. Yu, Y. Liu, M. Lin, S. H. Lim and Y. Zhou, *et al.*, *Sci. Rep.*, 2012, **2**, 754.
20 S. Fabiano, H. Usta, R. Forchheimer, X. Crispin, A. Facchetti and M. Berggren, *Adv. Mater.*, 2014, **26**, 7438–7443.
21 I. Meager, M. Nikolka, B. C. Schroeder, C. B. Nielsen, M. Planells, H. Bronstein, J. W. Rumer, D. I. James, R. S. Ashraf and A. Sadhanala, *et al.*, *Adv. Funct. Mater.*, 2014, **24**, 7109–7115.
22 T. Ma, K. Jiang, S. Chen, H. Hu, H. Lin, Z. Li, J. Zhao, Y. Liu, Y. M. Chang and C. C. Hsiao, *et al.*, *Adv. Energy Mater.*, 2015, **5**, 2–7.
23 V. Figa, C. Chiappara, F. Ferrante, M. P. Casaletto, F. Principato, S. Cataldo, Z. Chen, H. Usta, A. Facchetti and B. Pignataro, *J. Mater. Chem. C*, 2015, **3**, 5985–5994.
24 D. T. Chase, A. G. Fix, S. J. Kang, B. D. Rose, C. D. Weber, Y. Zhong, L. N. Zakharov, M. C. Lonergan, C. Nuckolls and M. M. Haley, *J. Am. Chem. Soc.*, 2012, **134**, 10349–10352.
25 J. Guo, D. Liu, J. Zhang, J. Zhang, Q. Miao and Z. Xie, *Chem. Commun.*, 2015, **51**, 12004–12007.
26 J. Kan, Y. Chen, D. Qi, Y. Liu and J. Jiang, *Adv. Mater.*, 2012, **24**, 1755–1758.
27 H. E. Katz, Z. Bao and S. L. Gilat, *Acc. Chem. Res.*, 2001, **34**, 359–369.
28 L. Zhang, A. Fonari, Y. Liu, A.-L. M. Hoyt, H. Lee, D. Granger, S. Parkin, T. P. Russell, J. E. Anthony and J.-L. Brédas, *et al.*, *J. Am. Chem. Soc.*, 2014, **136**, 9248–9251.
29 H. Hu, K. Jiang, J.-H. Kim, G. Yang, Z. Li, T. Ma, G. Lu, Y. Qu, H. Ade and H. Yan, *J. Mater. Chem. A*, 2016, 5039–5043.
30 A. Marrocchi, A. Facchetti, D. Lanari, S. Santoro and L. Vaccaro, *Chem. Sci.*, 2016, **7**, 6298–6308.
31 U. Sen, H. Usta, O. Acar, M. Citir, A. Canlier, A. Bozkurt and A. Ata, *Macromol. Chem. Phys.*, 2015, **216**, 106–112.
32 B. Servet, G. Horowitz, S. Ries, O. Lagorsse, P. Alnot, A. Yassar, F. Deloffre, P. Srivastava, R. Hajlaoui and P. Lang, *et al.*, *Chem. Mater.*, 1994, 1809–1815.
33 S. Allard, M. Forster, B. Souharce, H. Thiem and U. Scherf, *Angew. Chem., Int. Ed.*, 2008, **47**, 4070–4098.
34 H. Ebata, T. Izawa, E. Miyazaki, K. Takimiya, M. Ikeda, H. Kuwabara and T. Yui, *J. Am. Chem. Soc.*, 2007, **129**, 15732–15733.
35 L. Zhang, N. S. Colella, B. P. Cherniawski, S. C. B. Mannsfeld and A. L. Briseno, *ACS Appl. Mater. Interfaces*, 2014, **6**, 5327–5343.
36 M.-C. Chen, S. Vegiraju, C.-M. Huang, P.-Y. Huang, K. Prabakaran, S. L. Yau, W.-C. Chen, W.-T. Peng, I. Chao and C. Kim, *et al.*, *J. Mater. Chem. C*, 2014, **2**, 8892–8902.
37 N. D. Treat, J. A. Nekuda Malik, O. Reid, L. Yu, C. G. Shuttle, G. Rumbles, C. J. Hawker, M. L. Chabinyc, P. Smith and N. Stingelin, *Nat. Mater.*, 2013, **12**, 628–633.
38 M. Sawamoto, M. J. Kang, E. Miyazaki, H. Sugino, I. Osaka and K. Takimiya, *ACS Appl. Mater. Interfaces*, 2016, **8**, 3810–3824.
39 P.-Y. Huang, L.-H. Chen, Y.-Y. Chen, W.-J. Chang, J.-J. Wang, K.-H. Lii, J.-Y. Yan, J.-C. Ho, C.-C. Lee and C. Kim, *et al.*, *Chem. – Eur. J.*, 2013, **19**, 3721–3728.
40 Y. Yuan, G. Giri, A. L. Ayzner, A. P. Zoombelt, S. C. B. Mannsfeld, J. Chen, D. Nordlund, M. F. Toney, J. Huang and Z. Bao, *Nat. Commun.*, 2014, **5**, 3005.
41 J. Li, X. Qiao, Y. Xiong, W. Hong, X. Gao and H. Li, *J. Mater. Chem. C*, 2013, **1**, 5128.
42 R. Ponce Ortiz, H. Herrera, M. J. Mancheño, C. Seoane, J. L. Segura, P. Mayorga Burrezo, J. Casado, J. T. López Navarrete, A. Facchetti and T. J. Marks, *Chem. – Eur. J.*, 2013, **19**, 12458–12467.
43 L. Wang, X. Zhang, H. Tian, Y. Lu, Y. Geng and F. Wang, *Chem. Commun.*, 2013, **49**, 11272–11274.
44 J. Bai, Y. Liu, S. Oh, W. Lei, B. Yin, S. Park and Y. Kan, *RSC Adv.*, 2015, **5**, 53412–53418.
45 G. Lin, Y. Qin, J. Zhang, Y.-S. Guan, H. Xu, W. Xu and D. Zhu, *J. Mater. Chem. C*, 2016, **4**, 4470–4477.
46 Z. Fang, A. A. Eshbaugh and K. S. Schanze, *J. Am. Chem. Soc.*, 2011, **133**, 3063–3069.

47 G. E. Rudebusch, G. L. Espejo, J. L. Zafra, M. Peña-Alvarez, S. N. Spisak, K. Fukuda, Z. Wei, M. Nakano, M. A. Petrukhina and J. Casado, *et al.*, *J. Am. Chem. Soc.*, 2016, **138**, 12648–12654.
48 H. Usta, C. Risko, Z. Wang, H. Huang, M. K. Deliomeroglu, A. Zhukhovitskiy, A. Facchetti and T. J. Marks, *J. Am. Chem. Soc.*, 2009, **131**, 5586–5608.
49 M. Ozdemir, D. Choi, G. Kwon, Y. Zorlu, H. Kim, M.-G. Kim, S. Seo, U. Sen, M. Citir and C. Kim, *et al.*, *RSC Adv.*, 2016, **6**, 212–226.
50 M. J. Frisch, G. W. Trucks, H. B. Schlegel, G. E. Scuseria, M. A. Robb, J. R. Cheeseman, G. Scalmani, V. Barone, B. Mennucci, G. A. Petersson, H. Nakatsuji, M. Caricato, X. Li, H. P. Hratchian, A. F. Izmaylov, J. Bloino, G. Zheng, J. L. Sonnenberg, M. Hada, M. Ehara, K. Toyota, R. Fukuda, J. Hasegawa, M. Ishida, T. Nakajima, Y. Honda, O. Kitao, H. Nakai, T. Vreven, J. A. Montgomery, Jr., J. E. Peralta, F. Ogliaro, M. Bearpark, J. J. Heyd, E. Brothers, K. N. Kudin, V. N. Staroverov, T. Keith, R. Kobayashi, J. Normand, K. Raghavachari, A. Rendell, J. C. Burant, S. S. Iyengar, J. Tomasi, M. Cossi, N. Rega, J. M. Millam, M. Klene, J. E. Knox, J. B. Cross, V. Bakken, C. Adamo, J. Jaramillo, R. Gomperts, R. E. Stratmann, O. Yazyev, A. J. Austin, R. Cammi, C. Pomelli, J. W. Ochterski, R. L. Martin, K. Morokuma, V. G. Zakrzewski, G. A. Voth, P. Salvador, J. J. Dannenberg, S. Dapprich, A. D. Daniels, O. Farkas, J. B. Foresman, J. V. Ortiz, J. Cioslowski and D. J. Fox, *Gaussian 09, Revision C.01*, Gaussian, Inc., Wallingford CT, 2010.
51 C. Kim, A. Facchetti and T. J. Marks, *Adv. Mater.*, 2007, **19**, 2561–2566.
52 B. Kim, D. Y. Ryu, V. Pryamitsyn and V. Ganesan, *Macromolecules*, 2009, **42**, 7919–7923.
53 S. H. Park, H. S. Lee, J.-D. Kim, D. W. Breiby, E. Kim, Y. D. Park, D. Y. Ryu, D. R. Lee and J. H. Cho, *J. Mater. Chem.*, 2011, **21**, 15580.
54 G. Giri, E. Verploegen, S. C. Mannsfeld, S. Atahan-Evrenk, H. Kim do, S. Y. Lee, H. A. Becerril, A. Aspuru-Guzik, M. F. Toney and Z. Bao, *Nature*, 2011, **480**, 504.
55 D. S. Rampon, F. S. Rodembusch, J. M. F. M. Schneider, I. H. Bechtold, P. F. B. Gonçalves, A. A. Merlo and P. H. Schneider, *J. Mater. Chem.*, 2010, **20**, 715–722.
56 J. Peng, F. Zhai, X. Guo, X. Jiang and Y. Ma, *RSC Adv.*, 2014, **4**, 13078.
57 H. Usta, C. Newman, Z. Chen and A. Facchetti, *Adv. Mater.*, 2012, **24**, 3678–3684.
58 W. W. H. Wong, T. Birendra Singh, D. Vak, W. Pisula, C. Yan, X. Feng, E. L. Williams, K. L. Chan, Q. Mao and D. J. Jones, *et al.*, *Adv. Funct. Mater.*, 2010, **20**, 927–928.
59 L. Oldridge, M. Kastler and K. Müllen, *Chem. Commun.*, 2006, 885–887.
60 F. Uckert, S. Setayesh and K. Müllen, *Macromolecules*, 1999, **32**, 4519–4524.
61 Y. Diao, B. C.-K. Tee, G. Giri, J. Xu, D. H. Kim, H. a Becerril, R. M. Stoltenberg, T. H. Lee, G. Xue and S. C. B. Mannsfeld, *et al.*, *Nat. Mater.*, 2013, **12**, 665–671.
62 M. Gsänger, E. Kirchner, M. Stolte, C. Burschka, V. Stepanenko, J. Pflaum and F. Würthner, *J. Am. Chem. Soc.*, 2014, **136**, 2351–2362.
63 T. D. Anthopoulos, G. C. Anyfantis, G. C. Papavassiliou and D. M. De Leeuw, *Appl. Phys. Lett.*, 2007, **90**, 9–12.
64 Y. Zhou, S.-T. Han, P. Sonar, X. Ma, J. Chen, Z. Zheng and V. A. L. Roy, *Sci. Rep.*, 2015, **5**, 9446.
65 S.-H. Lee, D. Khim, Y. Xu, J. Kim, W.-T. Park, D.-Y. Kim and Y.-Y. Noh, *Sci. Rep.*, 2015, **5**, 10407.
66 T. B. Singh, P. Senkarabacak, N. S. Sariciftci, A. Tanda, C. Lackner, R. Hagelauer and G. Horowitz, *Appl. Phys. Lett.*, 2006, **89**, 1–3.
67 T. D. Anthopoulos, D. M. De Leeuw, E. Cantatore, S. Setayesh, E. J. Meijer, C. Tanase, J. C. Hummelen and P. W. M. Blom, *Appl. Phys. Lett.*, 2004, **85**, 4205–4207.
68 J.-Y. Hu, M. Nakano, I. Osaka and K. Takimiya, *J. Mater. Chem. C*, 2015, **3**, 4244–4249.
69 J. Kim, K. J. Baeg, D. Khim, D. T. James, J. S. Kim, B. Lim, J. M. Yun, H. G. Jeong, P. S. K. Amegadze and Y. Y. Noh, *et al.*, *Chem. Mater.*, 2013, **25**, 1572–1583.
70 H. Xu, Y. C. Zhou, X. Y. Zhou, K. Liu, L. Y. Cao, Y. Ai, Z. P. Fan and H. L. Zhang, *Adv. Funct. Mater.*, 2014, **24**, 2907–2915.
71 J. B. Kim, C. Fuentes-Hernandez, S. J. Kim, S. Choi and B. Kippelen, *Org. Electron. Phys. Mater. Appl.*, 2010, **11**, 1074–1078.
72 A. L. Patterson, *Phys. Rev.*, 1939, **56**, 978–982.
73 N. S. Colella, L. Zhang, T. McCarthy-Ward, S. C. B. Mannsfeld, H. H. Winter, M. Heeney, J. J. Watkins and A. L. Briseno, *Phys. Chem. Chem. Phys.*, 2014, 3–7.
74 D. Niedzialek, V. Lemaur, D. Dudenko, J. Shu, M. R. Hansen, J. W. Andreasen, W. Pisula, K. Müllen, J. Cornil and D. Beljonne, *Adv. Mater.*, 2013, **25**, 1939–1947.